Supplement of Atmos. Chem. Phys. Discuss., 14, 15895–15951, 2014
http://www.atmos-chem-phys-discuss.net/14/15895/2014/
doi:10.5194/acpd-14-15895-2014-supplement

Atmospheric Chemistry and Physics Discussions
Open Access

Supplement of

Kerb and urban increment of highly time-resolved trace elements in PM_{10}, $PM_{2.5}$ and $PM_{1.0}$ winter aerosol in London during ClearfLo 2012

S. Visser et al.

Correspondence to: M. Furger (markus.furger@psi.ch)

Supplement A: RDI backup filter and $PM_{1.0}$ cut off analysis

RDI backup filter analysis

RDI backup filters (Balston 050-11-BQ 2 µm, microfiber, fluorocarbon resin binder) from the ClearfLo winter campaign were immersed in water and sonicated for about 1.5 hrs. One filter per measurement site was available. Total sulphate (SO_4^{2-}) mass was obtained by analysing the solutions with ion chromatography and converted to concentrations by dividing by the total air volume that passed through the filter during the campaign.

Table S1 compares the S concentrations from the RDI $PM_{1.0-0.3}$ stage with S (from SO_4^{2-}) collected by the backup filter. The sum of both (Total S <1µm) is compared with S from AMS sulphate measurements. The ratio in the last column reveals mass-closure between the RDI and AMS within 20%.

Table S1. Comparison between S from RDI $PM_{1.0-0.3}$ fractions and backup filters (S from SO_4^{2-}) with S from the AMS (S from SO_4). Units in ng m^{-3}. The ratio of S in the RDI to the AMS is given in the last column (ratio of RDI Total S <1 µm to AMS S).

Site	RDI $PM_{1.0-0.3}$ S	S in backup filter	Total S <1 µm	AMS S	Ratio RDI : AMS
MR	178	398	576	476	**1.21**
NK	159	405	564	607	**0.93**
DE	212	359	571	715	**0.80**

RDI $PM_{1.0}$ cut off analysis

As noted in the main text, elements whose mass is dominated by the $PM_{1.0}$ fraction are typically underestimated by RDI-SR-XRF relative to external measurements like the AMS and 24-hr filter measurements. One explanation is that the collection efficiency of the RDI $PM_{1.0}$ stage is smaller than expected, e.g. by a larger-than-expected size cut off. We therefore performed new laboratory measurements of the RDI size-dependent collection efficiency, and compare to earlier characterisations by Bukowiecki et al. (2009) and Richard et al. (2010).

Figure S1 shows the setup used for the collection efficiency measurements. $(NH_4)_2SO_4$, NH_4NO_3 and NaCl particles were nebulized, dried and size-selected using a differential mobility analyser (DMA, TSI, Inc., Shoreview, MN, USA), and then sampled with the RDI. The DMA was operated with sample and sheath flow rates of 0.3 and 3.0 L min^{-1}, respectively. A condensation particle counter (CPC1, TSI, Inc., Shoreview, MN, USA) with a flow rate of 1.0 L min^{-1} was continuously connected at the inlet stage of the RDI to measure the particles entering the RDI, and to correct for fluctuations in nebulizer performance. A second line led to an additional CPC (CPC2, 1 L min^{-1}) and an Aerodyne aerosol mass spectrometer (AMS, Aerodyne Research, Inc., Billerica, MA, USA) with a flow rate of 0.1 l min^{-1}. This line could be connected at the inlet, after the $PM_{2.5-1.0}$ (B) stage or after the $PM_{1.0-0.3}$ (C) stage. Measurements following the B and C stages were made by connecting the line to a small hole in the lid covering these stages, resulting in sampling of the air flow at a 90° angle (see picture in Figure S1). The total flow through the system was controlled by a mass flow controller connected to a clean air generator pumping air into the nebulizer and RDI simultaneously. The RDI was operated using three wheels with freshly mounted 6-µm polypropylene foils coated with Apiezon to minimize particle bouncing effects, to simulate ambient field measurements. Tests ruled out differences in measurements on the top or bottom side of the lid at the B and C stages. For the final results, all data was collected at the bottom side of the B and C stages.

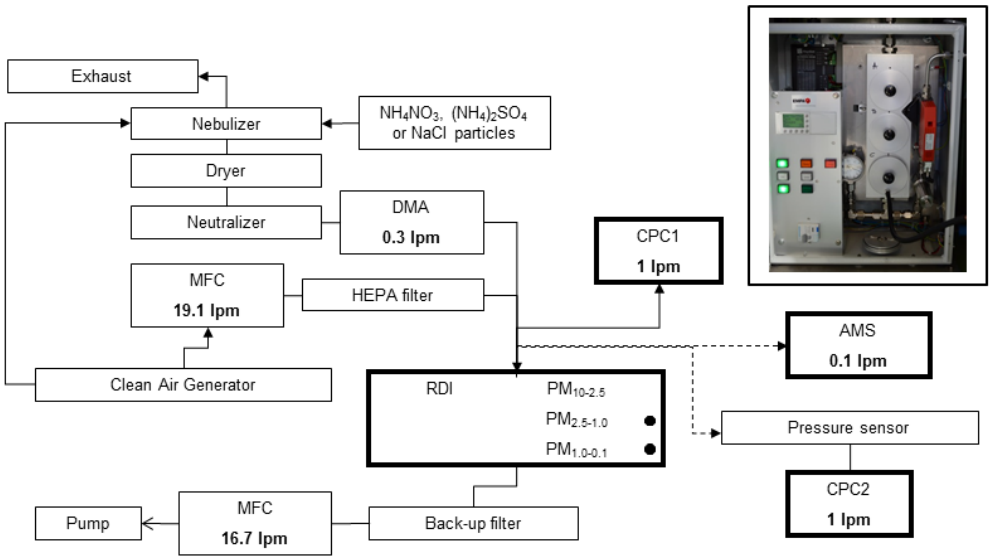

Figure S1. Setup of the collection efficiency measurements of the RDI PM_1 impactor stage. The line with the AMS and CPC2 was connected at the inlet,

after the $PM_{2.5-1.0}$ or after the $PM_{1.0-0.3}$ stage. The picture of the RDI shows the connection at the bottom side of the lid of the $PM_{1.0-0.3}$ stage.

As noted above, measurements were conducted at the RDI inlet, after the B stage impactor (nominal size cut = 1.0 µm) and after the C stage impactor (nominal size cut = 0.1 µm). RDI collection efficiency at each stage is defined as 1 minus transmission. To correct for fluctuations in nebulizer concentrations, all data for a given set of CPC2/AMS measurements were normalized to a constant inlet (CPC1) concentration. Transmission from the inlet across the B stage impactor was between 90 and 100% for all sizes (aerodynamic diameter D_a < 950 nm), indicating negligible particle losses and/or unintended collection of small particles. C stage collection efficiency (CE_C) was therefore calculated using Eq. (S1):

$$\boldsymbol{CE_C = 1 - \left(Conc_C * \frac{CPC1_{ref}}{CPC1_{measC}}\right) / \left(Conc_B * \frac{CPC1_{ref}}{CPC1_{measB}}\right)}$$

(S1)

Concentrations were measured using both CPC2 and the AMS. For large particles, where the fraction of multiple charged particles passed by the DMA is negligible, these two methods yield similar results. For smaller particles, collection efficiency as calculated by the CPC2 is biased low due to the presence of multiple charged particles with larger diameters, as clearly evidenced from AMS size distributions. For simplicity, we therefore present only the AMS results here. RDI collection efficiencies are calculated by fitting a lognormal distribution to each mode and using the resulting mass concentrations in Eq. S 1. This allows simultaneous calculation of RDI collection efficiencies for several sizes, providing an internal consistency and stability check for the measurements.

Figure S2 shows the collection efficiency of the $PM_{1.0-0.3}$ (C stage) nozzle for two RDIs (RDI1 and RDI2) as a function of D_a for NH_4NO_3 particles. D_a is calculated from AMS size measurements, assuming a density of 1.74 and a Jayne shape factor (DeCarlo et al., 2004) of 0.8. Cut points are estimated by a sigmoidal fit to the collection efficiency curves, and yield different cut points for the two RDIs. RDI1 has a cut point of 290 ± 25 nm and RDI2 a cut point of 410 ± 15 nm. This discrepancy was investigated using RDI2 equipped with the $PM_{1.0-0.3}$ nozzle of RDI1 (RDI2 (nozzle RDI1)), demonstrating that the difference between the two RDIs is governed by

nozzle performance, because the cut point of this system is 300 ± 20 nm and therefore closer to the RDI1 performance. Similar cut points for the various systems were obtained using $(NH_4)_2SO_4$ and NaCl particles (not shown).

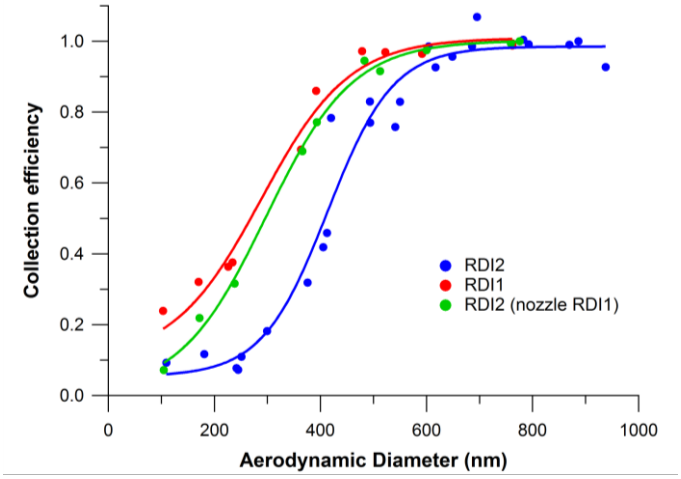

Figure S2. Collection efficiency of the RDI $PM_{1.0\text{-}0.3}$ impactor stage as a function of aerodynamic diameter.

Measurements of the nozzle sizes under a microscope reveal small differences between the RDIs. A 1.0 µm cut point at the B stage impactor is obtained with a nozzle size of 0.68 x 10 mm. The RDI1 and RDI2 B stage nozzles were 0.70 x 10 mm, and a third RDI that was used at Marylebone Road during ClearfLo had a size of 0.71 x 10 mm. The C stage nozzle size should measure 0.30 x 10 mm for a cut point of 0.1 µm. However, the nozzle sizes were 0.30-0.31 x 10, 0.30-0.32 x 10 and 0.32 x 10 for RDI1, RDI2 and the third RDI, respectively. We expect the deviations from these measurements from the machining of the nozzles, resulting in higher cut points than expected for the $PM_{1.0}$ stage, and possibly also for the $PM_{2.5\text{-}1.0}$ stage.

Conclusions

The $PM_{1.0\text{-}0.3}$ collection efficiency curves are different for the two RDIs. RDI2 has a larger small-end cut point of 410 ± 15 nm than RDI1 of 290 ± 25 nm. RDI2 with the $PM_{1.0\text{-}0.3}$ nozzle of RDI1 resulted in a similar cut point of RDI1 of 300 ± 20 nm. The slightly larger nozzles than theoretically calculated are the likely reason for the observed increase in the small-end cut point of the $PM_{1.0\text{-}0.3}$ nozzle and thus in reduced particle collection at the C stage.

Supplement B: Additional tables and figures

Table S2. Fit coefficients and Pearson's R values for elements measured with the RDI ($PM_{10-2.5}$, $PM_{2.5-1.0}$ and $PM_{1.0-0.3}$ fractions summed to total PM_{10} and averaged to 24 hrs) relative to 24-hr PM_{10} filter measurements. Data points were fitted with an orthogonal fit and forced zero intercept.

Element	Fit coefficient	Pearson's R
Na	1.98	0.87
Mg	2.19	0.99
Al	1.79	0.88
K	0.52	0.78
Ca	0.78	0.94
Ti	1.04	0.86
V	0.17	0.64
Cr	0.41	0.29
Mn	1.49	0.91
Fe	0.93	0.96
Ni	0.82	0.56
Cu	1.33	0.94
Zn	0.71	0.94
Sr	1.49	0.74
Mo	2.93	0.86
Sn	0.43	0.97
Sb	1.44	0.90
Ba	1.67	0.91
Pb	0.41	0.53

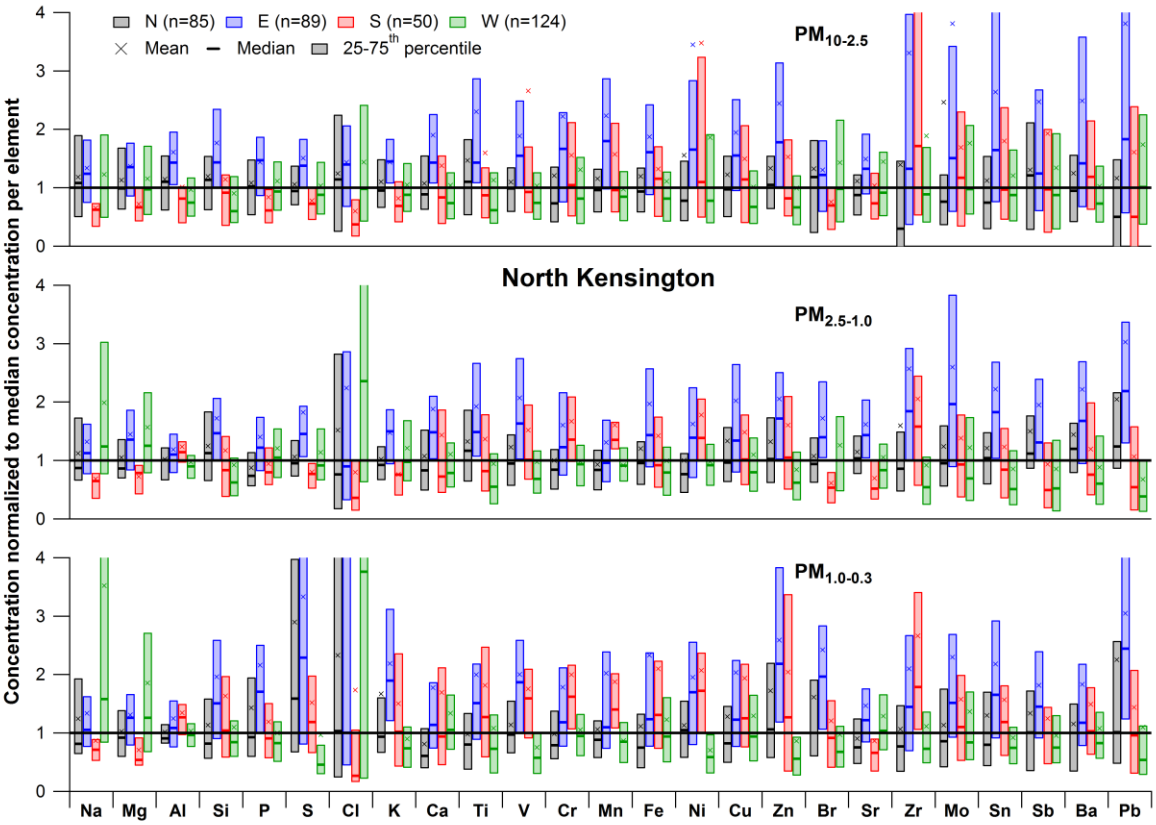

Figure S3. Same as Figure 5, but for NK with mean, median and 25-75th percentile trace element concentrations split in four wind direction sectors (N, E, S, W) normalized to the global median concentration per element for $PM_{10-2.5}$ (top), $PM_{2.5-1.0}$ (middle) and $PM_{1.0-0.3}$ (bottom). See section 4.2.2 for the definition of the wind direction sectors.

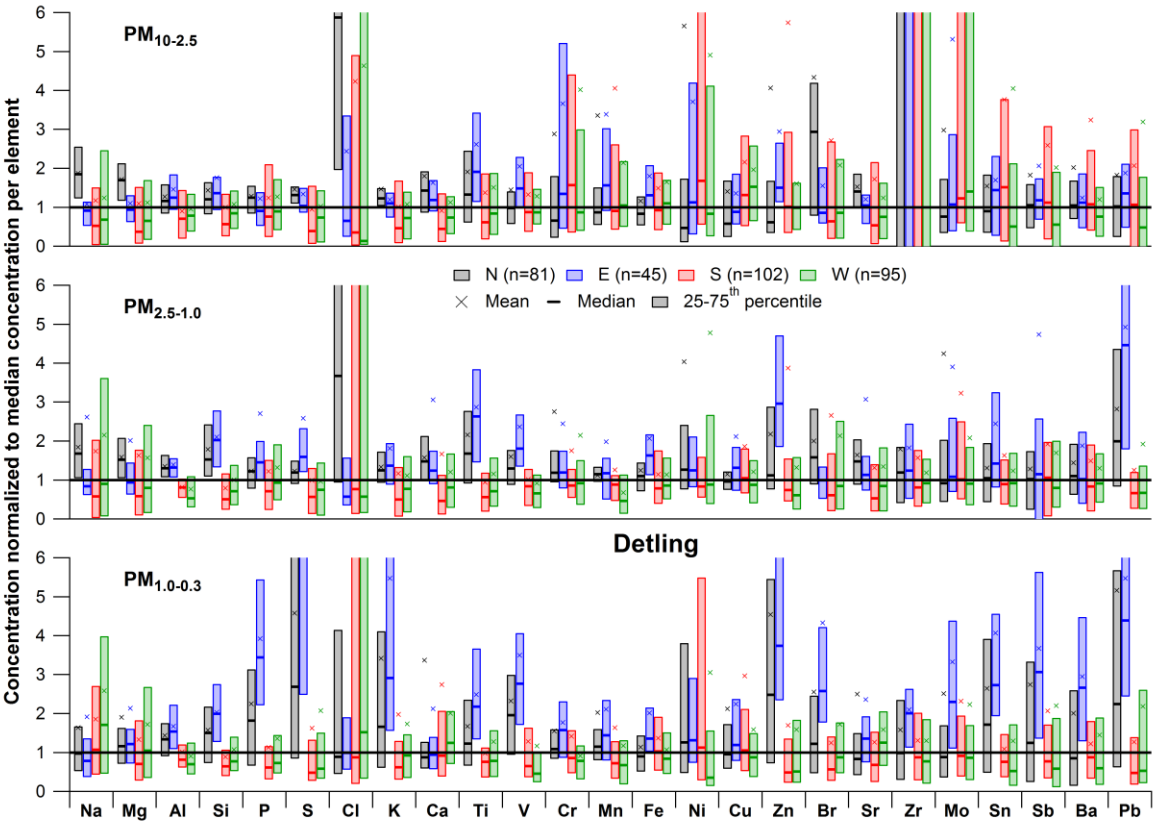

Figure S4. Same as Figure 5, but for DE with mean, median and 25-75th percentile trace element concentrations split in four wind direction sectors (N, E, S, W) normalized to the global median concentration per element for $PM_{10-2.5}$ (top), $PM_{2.5-1.0}$ (middle) and $PM_{1.0-0.3}$ (bottom). See section 4.2.2 for the definition of the wind direction sectors.

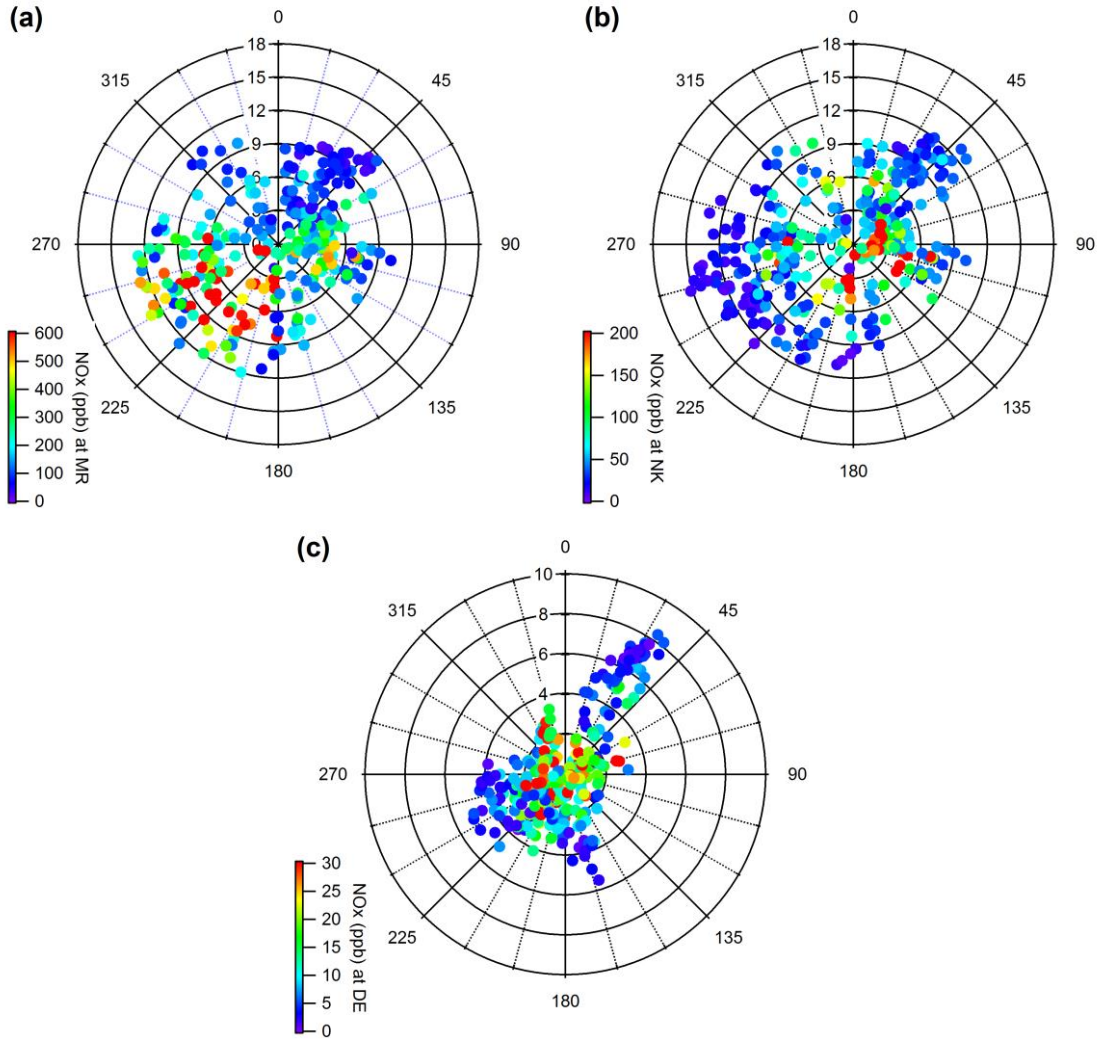

Figure S5. Wind roses as a function of wind direction (angle) and wind speed (diameter) at (a) BT Tower, color-coded by NO_x concentrations at MR, (b) BT Tower, color-coded by NO_x concentrations at NK, (c) DE, color-coded by NO_x concentrations at DE for the RDI sampling periods (see Table 1).

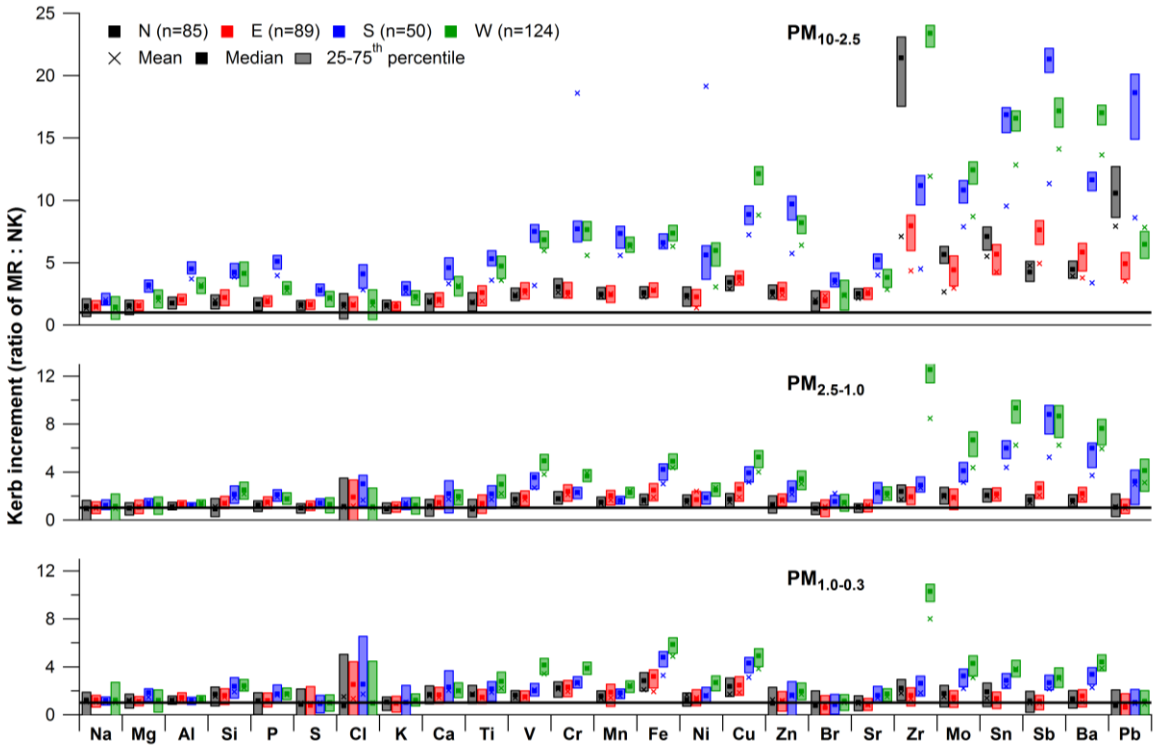

Figure S6. Same as Figure 6, but with mean, median and 25-75th percentile kerb increment values for trace elements at MR relative to NK for $PM_{10-2.5}$ (top), $PM_{2.5-1.0}$ (middle) and $PM_{1.0-0.3}$ (bottom) split in N, E, S and W wind sectors. See section 4.2.2 for the definition of the wind direction sectors.

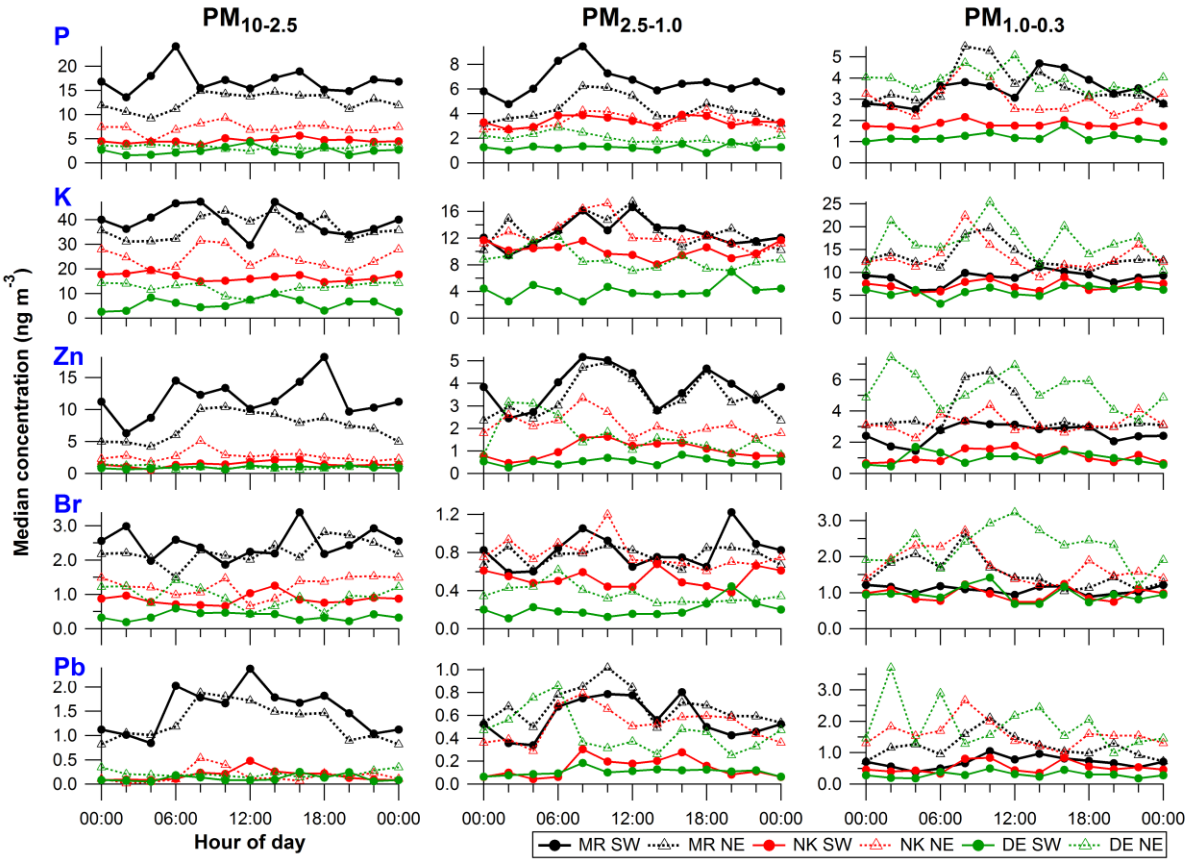

Figure S7. Same as Figure 7, but for all other elements: P, K, Br, Zn, Pb (regional background); Mg (sea salt), Al, Ca, Ti, Sr (mineral dust); Cl (sea salt), V, Cr, Mn, Ni (traffic-related); Cu, Zr, Mo, Sn, Ba (brake wear). Diurnal cycles of 2-hr median concentrations for $PM_{10\text{-}2.5}$ (left), $PM_{2.5\text{-}1.0}$ (middle) and $PM_{1.0\text{-}0.3}$ (right) at MR, NK, DE split in SW and NE wind sectors. See section 4.2.2 for the definition of the wind direction sectors. Hour of day is start of 2-hr sampling period, so 00:00 means sampling from 00:00 to 02:00.

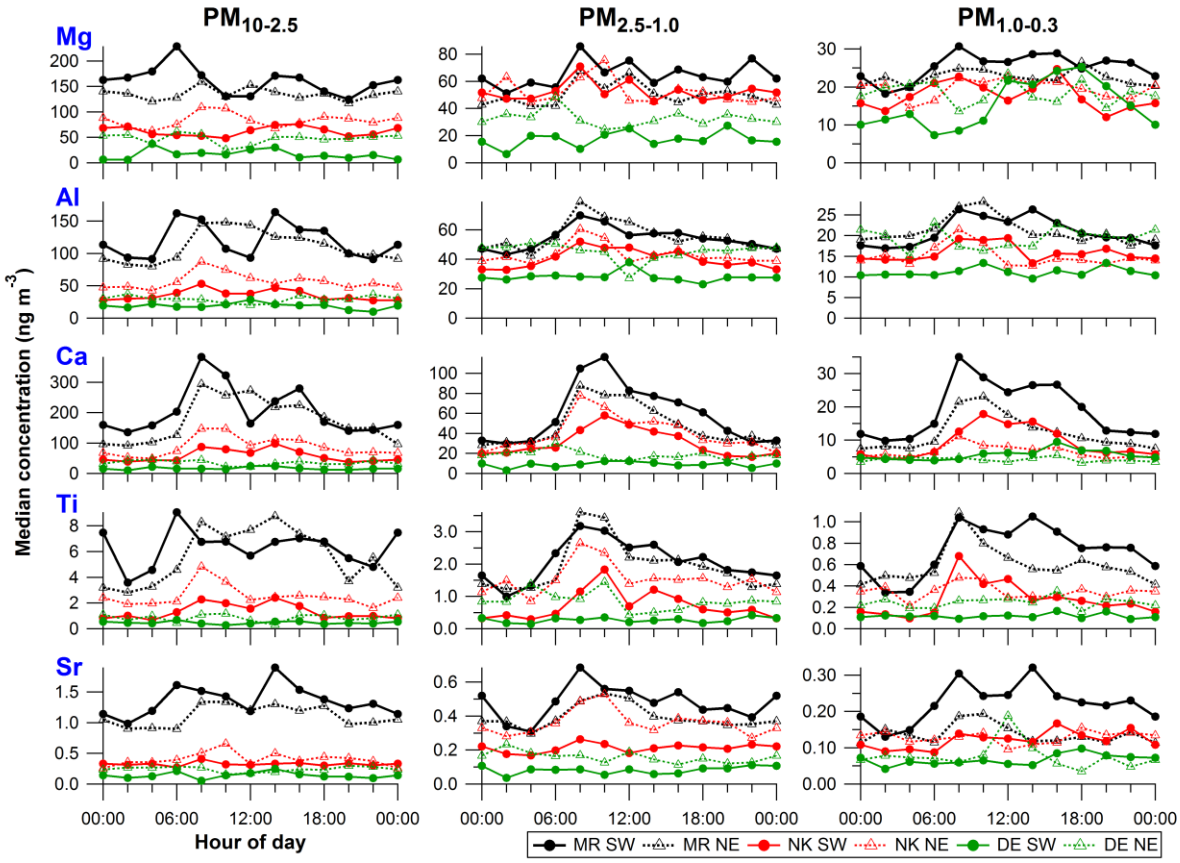

(Figure S7, continued)

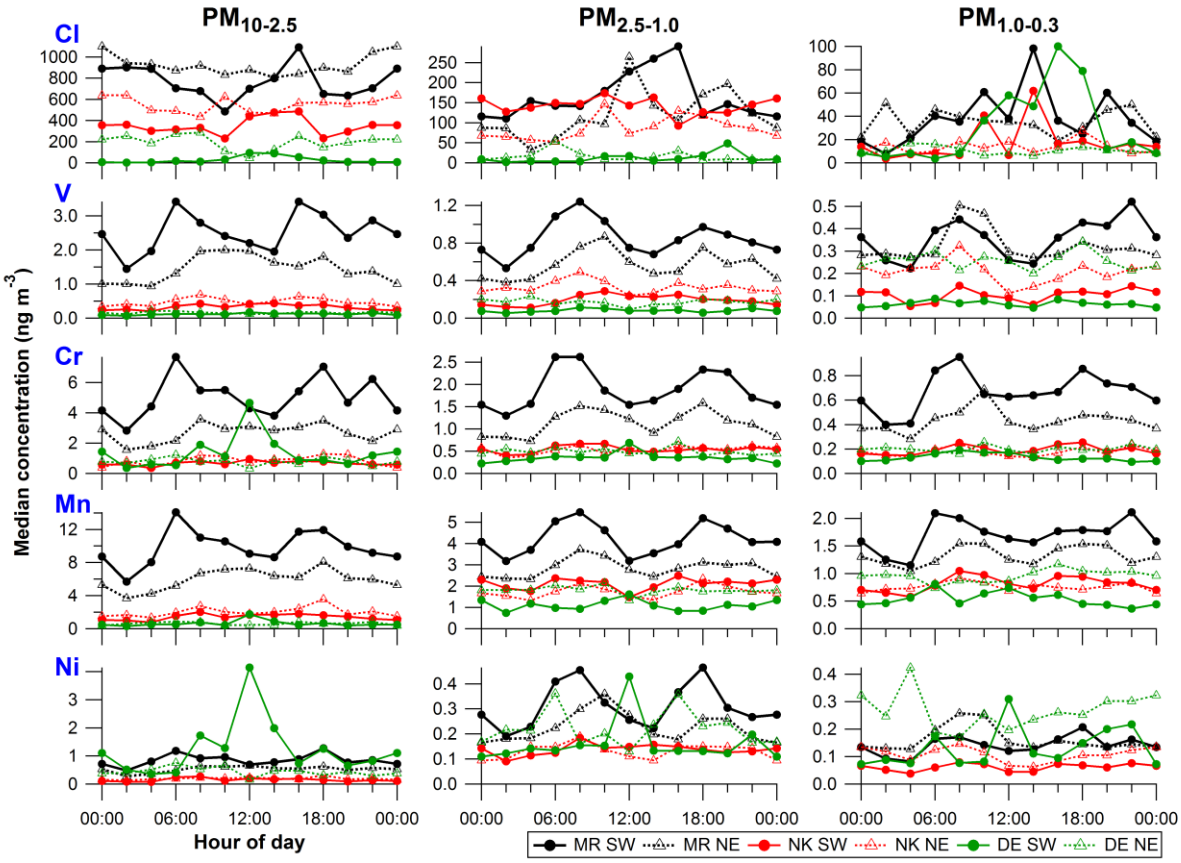

(Figure S7, continued)

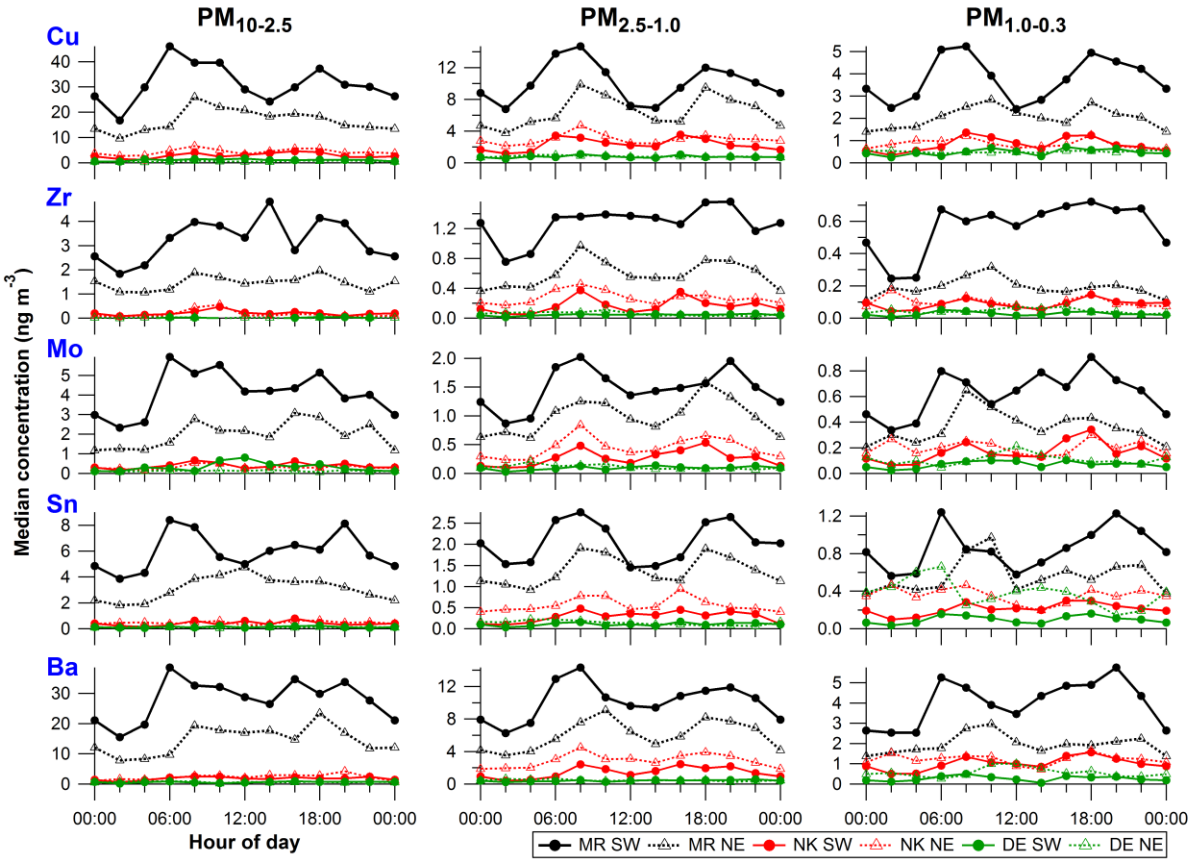

(Figure S7, continued)

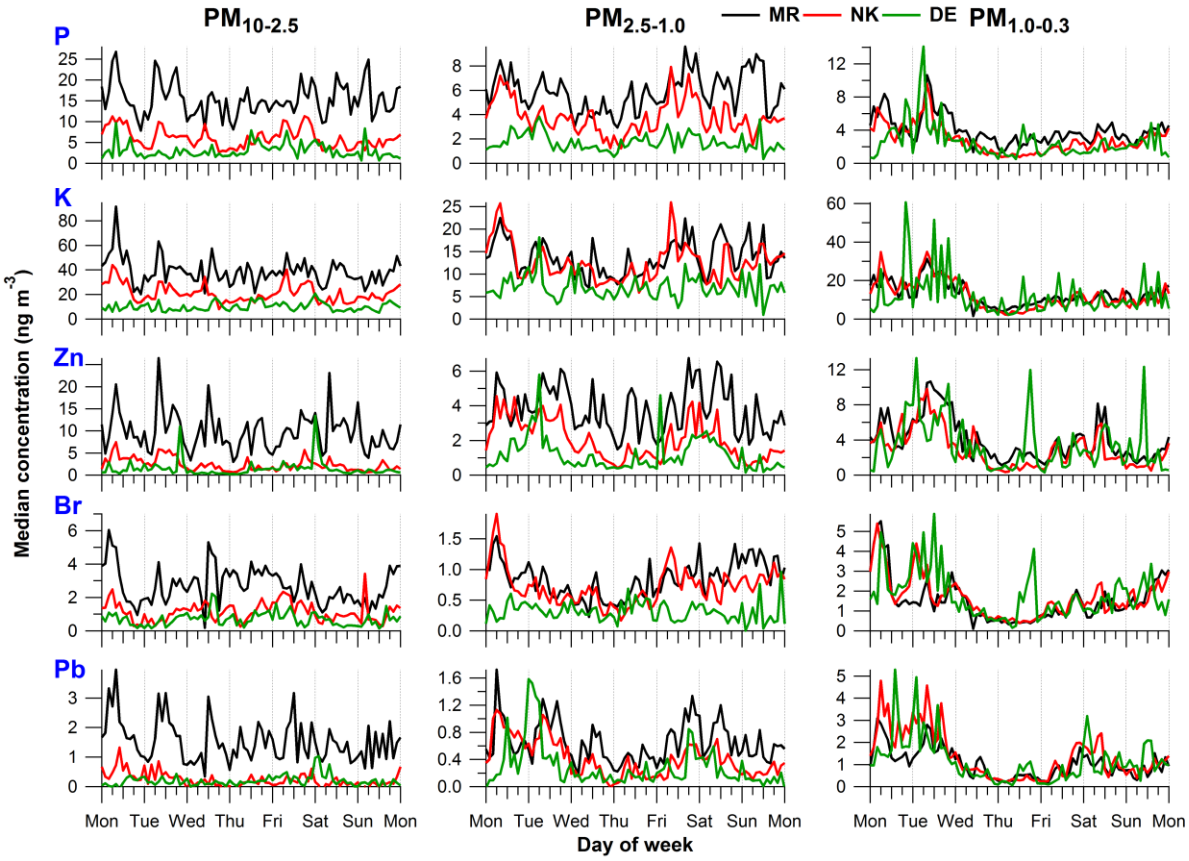

Figure S8. Same as Figure 8, but for all other elements: P, K, Br, Zn, Pb (regional background); Mg (sea salt), Al, Ca, Ti, Sr (mineral dust); Cl (sea salt), V, Cr, Mn, Ni (traffic-related); Cu, Zr, Mo, Sn, Ba (brake wear). Weekly cycles of 2-hr median concentrations for $PM_{10\text{-}2.5}$ (left), $PM_{2.5\text{-}1.0}$ (middle) and $PM_{1.0\text{-}0.3}$ (right) at MR, NK, DE.

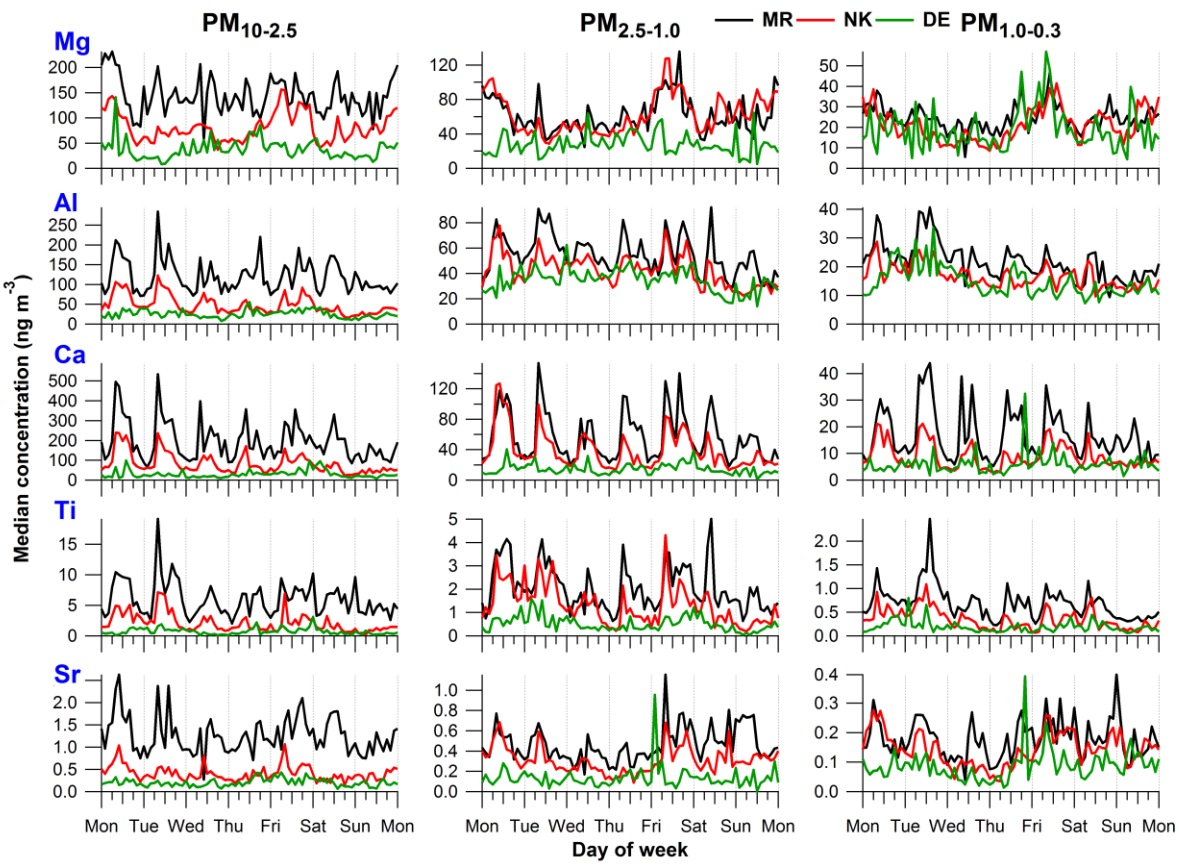

(Figure S8, continued)

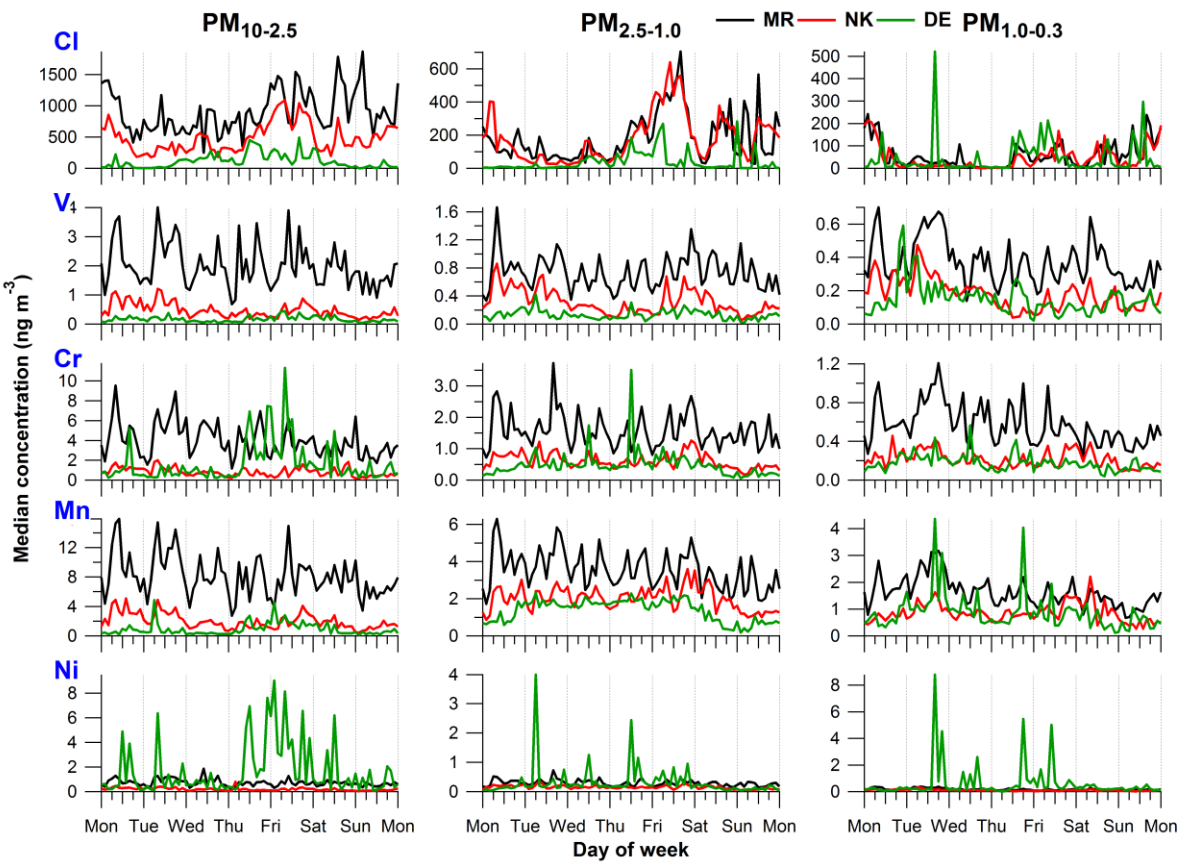

(Figure S8, continued)

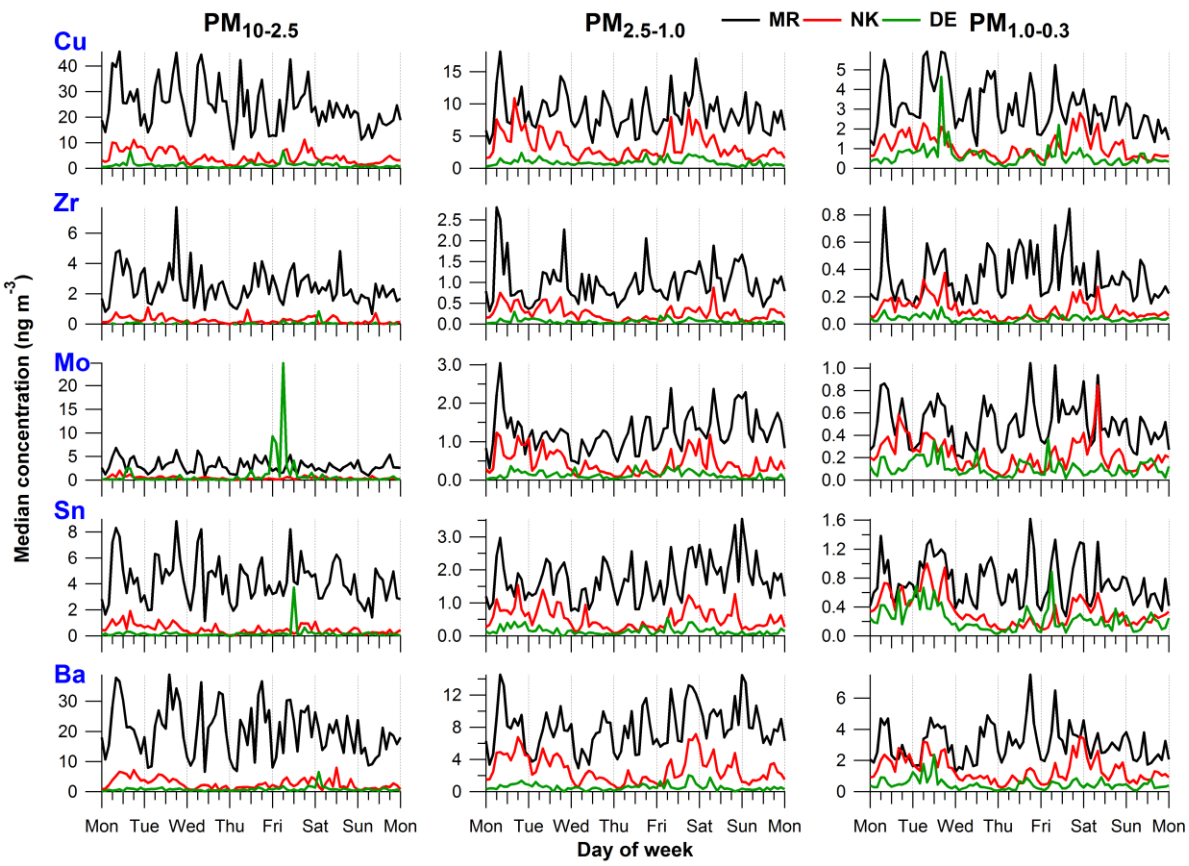

(Figure S8, continued)

References

Bukowiecki, N., Richard, A., Furger, M., Weingartner, E., Aguirre, M., Huthwelker, T., Lienemann, P., Gehrig, R., and Baltensperger, U.: Deposition uniformity and particle size distribution of ambient aerosol collected with a rotating drum impactor, Aerosol Sci. Technol., 43, 891-901, 2009.

DeCarlo, P. F., Slowik, J. G., Worsnop, D. R., Davidovits, P., and Jimenez, J. L.: Particle morphology and density characterization by combined mobility and aerodynamic diameter measurements. Part 1: Theory, Aerosol Sci. Technol., 38, 1185-1205, 10.1080/027868290903907, 2004.

Richard, A., Bukowiecki, N., Lienemann, P., Furger, M., Fierz, M., Minguillon, M. C., Weideli, B., Figi, R., Flechsig, U., Appel, K., Prevot, A. S. H., and Baltensperger, U.: Quantitative sampling and analysis of trace elements in atmospheric aerosols: impactor characterization and synchrotron-XRF mass calibration, Atmos. Meas. Tech., 3, 1473-1485, 2010.